Experimental validation of coil phase parametrisation on ASDEX Upgrade, and extension to ITER

D A Ryan[1 2], Y Q Liu[3], A Kirk[1], W Suttrop[4], B Dudson[2], M Dunne[4], M Willensdorfer[4], the ASDEX-Upgrade team[4] and the EUROfusion MST1 team[1]

[1] CCFE, Culham Science Centre, Abingdon, Oxfordshire, UK

[2] York Plasma Institute, Department of Physics, University of York, Heslington, York, UK

[3] General Atomics, P. O. Box 85608, San Diego, California 92186-5608, USA

[4] Max Planck Institute for Plasma Physics, Garching, Germany

Abstract. It has been previously demonstrated in (Li *et al* 2016 *Nuclear Fusion* **56** 126007) that the optimum upper/lower coil phase shift $\Delta\Phi_{opt}$ for alignment of RMP coils for ELM mitigation depends sensitively on q_{95}, and other equilibrium plasma parameters. Therefore, $\Delta\Phi_{opt}$ is expected to vary widely during the current ramp of ITER plasmas, with negative implications for ELM mitigation during this period. A previously derived and numerically benchmarked parametrisation of the coil phase for optimal ELM mitigation on ASDEX Upgrade (Ryan *et al* 2017 *Plas. Phys. Cont. Fus.* **59** 024005) is validated against experimental measurements of $\Delta\Phi_{opt}$, made by observing the changes to the ELM frequency as the coil phase is scanned. It is shown that the parametrisation may predict the optimal coil phase to within 32 degrees of the experimental measurement for $n = 2$ applied perturbations. It is explained that this agreement is sufficient to ensure that the ELM mitigation is not compromised by poor coil alignment. It is also found that the phase which maximises ELM mitigation is shifted from the phase which maximizes density pump-out, in contrast to theoretical expectations that ELM mitigation and density pump out have the same $\Delta\Phi_{ul}$ dependence. A time lag between the ELM frequency response and density response to the RMP is suggested as the cause. The method for numerically deriving the parametrisation is repeated for the ITER coil set, using the baseline scenario as a reference equilibrium, and the parametrisation coefficients given for future use in a feedback coil alignment system. The relative merits of square or sinusoidal toroidal current waveforms for ELM mitigation are briefly discussed.

1. Introduction

Edge Localised Modes (ELMs) - a quasi periodic MHD instability - are ubiquitous in current tokamaks during H-mode operation[2, 3]. Studies suggest that at the scale of ITER, ELMs may cause unacceptable erosion of plasma facing components, hindering the scientific objectives of the machine[4]. It is also well known that by applying Resonant Magnetic Perturbations (RMPs), usually using dedicated ELM control coils, ELMs may be triggered prematurely during the build-up phase of the ELM cycle when the pressure pedestal is lower[5], resulting in a smaller heat load to the divertor[6]. By this mitigation mechanism, ELM heat loads may potentially be reduced below the material damage threshold[7]. However, it is also commonly observed that mitigation is accompanied by a reduction in particle confinement resulting in a drop in the plasma density profile, termed density pump out[8]. ELM mitigation has now been demonstrated in most major tokamaks[1, 9, 10, 11, 12, 5, 13], and a set of ELM control coils will be installed on ITER[14]. While a robust predictive theory of ELM mitigation is currently lacking, sufficient experimental and numerical observations have been made to allow certain optimisations of the applied RMPs. Namely, correlations have been established between the mitigated ELM frequency f_{ELM}, and the outermost resonant component of the applied field $|b^1_{res}|$, computed including the plasma response to the applied field[15, 16]. Here $|b^1|$ refers to absolute value of the normal component of the perturbed magnetic field in the dimensionless unit defined as $|b^1| = |\frac{\mathbf{b}\cdot\nabla\psi}{\mathbf{B_{eq}}\cdot\nabla\phi}\frac{q}{R_0^2 B_0}|$, while $|b^1_{res}|$ is the pitch resonant component of this quantity (ie, poloidal harmonic m chosen such that $m = nq$) evaluated at the outermost rational surface included in the simulation. Meanwhile, an experimental correlation has been established between the maximum plasma surface displacement in the region of the X point ξ_X and the occurrence of density pump out[17], and a numerical correlation has been established between $|b^1_{res}|$ and ξ_X[18]. These two observations suggest that maximising the mitigated ELM frequency, also inevitably maximises the density pump out. Many tokamaks have both an upper and a lower set of RMP coils, which permits the applied field to be tuned by introducing a shift between the phase of the upper toroidal current waveform Φ_{upper}, and the phase of the lower toroidal current waveform Φ_{lower}, defined here as $\Delta\Phi_{ul} = \Phi_{upper} - \Phi_{lower}$. It has been shown numerically that $|b^1_{res}|$ is sensitive to $\Delta\Phi_{ul}$[19, 20], and experimentally that a corresponding sensitivity exists in f_{ELM}[15]. Therefore, for a given plasma equilibrium an applied field may be tuned to maximise ELM mitigation by tuning $\Delta\Phi_{ul}$ to some optimal phase, $\Delta\Phi_{opt}$, which can be computed by numerically scanning $\Delta\Phi_{ul}$ to maximise $|b^1_{res}|$. It is well known that $|b^1_{res}|$ may be drastically altered by the plasma response to the applied perturbation, which must be accounted for. In this work the plasma response is computed using the MARS-F code[21], which solves the linearised equations of resistive MHD in realistic toroidal geometry including toroidal rotation.

This work will frequently refer to the optimal coil phase, often with slightly different meaning depending on context. In a numerical context, $\Delta\Phi_{opt}$ is defined as the coil phase shift which maximises the outermost resonant component of the total magnetic perturbation, $|b^1_{res}|$.

coeff	a	b	c	d	e	f	g	h	i
n=1 total	0.43305	-5.7	17.097	-2.7405	29.94	-99.267	-0.45866	49.966	-210.18
n=2 total	0.14047	1.7732	-8.5336	-0.33719	-22.025	63.892	-3.1757	129.07	-286.34

Table 1. Coefficients of the 2D quadratic parametrisation of $\Delta\Phi_{opt}$ (equation 1), for the cases which are experimentally validated in this work: $n = 1, 2$ applied fields, including plasma response (ie, the total field). The parametrisation and coefficients were produced in [22], where the $n = 3, 4$ and vacuum cases are also listed.

In an experimental context, $\Delta\Phi_{opt,ELM}$ is here defined as the coil phase which maximises the mitigated ELM frequency, while $\Delta\Phi_{opt,ne}$ is the coil phase which maximises the density pump out effect.

In a recent work, of which this work is a logical extension, a numerical parametrisation was developed for $\Delta\Phi_{opt}$ for ASDEX Upgrade plasmas, based on the edge safety factor q_{95} and normalised plasma pressure β_N[22]. This parametrisation is a 2D quadratic in q_{95} and β_N, reproduced here in equation 1, with coefficient values listed in table 1.

$$\Delta\Phi_{opt,quad} = a(x^2y^2) + b(x^2y) + c(x^2) + d(xy^2) + e(xy) + f(x) + g(y^2) + h(y) + i \quad (1)$$

This parametrisation was benchmarked against computations of $\Delta\Phi_{opt}$ made using MARS-F for a set of benchmarking points, each consisting of a free boundary equilibrium and kinetic profiles reconstructed from experimental measurements, and experimentally applied RMP coil currents. In this work, $\Delta\Phi_{opt,ELM}$ and $\Delta\Phi_{opt,ne}$ are experimentally measured by observing the modulation of ELM frequency and density as $\Delta\Phi_{ul}$ is scanned. The uncertainty for each discharge is calculated by treating $0 \rightarrow 2\pi$ cycles in $\Delta\Phi_{ul}$ as repeat measurements for each discharge, implicitly assuming that $\Delta\Phi_{opt,ELM}$ and $\Delta\Phi_{opt,ne}$ are constant in each discharge. The basis of this assumption is that the flattops studied here contain only very minor changes to q_{95}, and although the β_N variation may be large, the dependence of the optimal coil phase on β_N is much weaker than on q_{95}. In [22], plasma shape fluctuations were identified as the most likely candidate for the main source of uncertainty of the $\Delta\Phi_{opt}$ parametrisation. Because of this the error in $\Delta\Phi_{opt,ELM}$ and $\Delta\Phi_{opt,ne}$ due to fluctuations in q_{95} or β_N which occur during the flattops of the discharges studied here, is expected to be small compared to random error or error due to plasma shape fluctuations, and is neglected. It is found that $\Delta\Phi_{opt,ne}$ is shifted upwards relative to $\Delta\Phi_{opt,ELM}$. It is suspected the shift is caused by a time lag in the density response to the RMP relative to the ELM frequency response, due to the relatively slow particle transport timescale. A validation of the previously derived 2D parametrisation is performed against the direct experimental measurements of $\Delta\Phi_{opt,ELM}$. It is shown that for $n = 2$ discharges the accuracy is sufficient for ELM mitigation optimisation, however for $n = 1$ discharges the uncertainty was greater due to the smaller number of relevant $n = 1$ discharges available. The parametrisation of $\Delta\Phi_{opt}$ is then re-derived for the

ITER ELM coil set, and the coefficients stated here for future use in guiding experiments, or in a coil alignment feedback algorithm.

In ELM control experiments, the current waveform in toroidal angle ϕ may be chosen to be either rectangular or sinusoidal. In a brief discussion, it is explained that rectangular toroidal waveforms are expected to yield superior ELM control compared to sinusoidal, even accounting for their inability to achieve precise alignment. Regardless, other experimental considerations may necessitate the use of sinusoidal waveforms.

2. Parametrisation Experimental Validation

In order to validate the previously developed[22] 2D quadratic parametrisation of the optimal coil phase, it must be compared with direct experimental measurements. In this section, the 2D quadratic and MARS-F optimal coil phase predictions are compared with experimental measurements to provide direct validation. Previously performed experiments in which $\Delta\Phi_{ul}$ was scanned and a varying mitigated ELM frequency was observed, were gathered from the experimental database of the ASDEX Upgrade tokamak. The optimum coil phases for ELM mitigation and density pump out are extracted from these coil phase scan experiments on ASDEX Upgrade, and these coil phases are then compared with predictions of full MARS-F modelling, and the 2D quadratic parametrisation.

2.1. Coil Phase Scan Experiments

The ELM coils of ASDEX Upgrade are powered by multiple independent power supply units, allowing the coil phase to be scanned by applying sinusoidally time varying currents to the coils, such that the toroidal waveform of the current in the upper coil set moves relative to the waveform in the lower set as in [23]. Figure 1 plots the coil currents, ELM frequency and density of discharge number 33143, in which the coil phase is scanned through several complete 2π cycles, and f_{elm} and n_e are modulated by the changing coil phase. From experiments such as this, $\Delta\Phi_{opt,ELM}$ and $\Delta\Phi_{opt,ne}$ may be measured. Table 2 summarises the discharges of the ASDEX Upgrade tokamak used in this study.

2.2. Extracting Experimental $\Delta\Phi_{opt}$

Two experimental optimum phases are measured, $\Delta\Phi_{opt,ELM}$ and $\Delta\Phi_{opt,ne}$, which are the experimental phases at which the ELM frequency and density pump out respectively are maximised. To extract $\Delta\Phi_{opt,ELM}$ and $\Delta\Phi_{opt,ne}$, the time domains of each studied discharge are first divided into complete $(0 \rightarrow 2\pi)$ cycles of $\Delta\Phi_{ul}$. In this work, density pump out Δn_e is defined relative to a locally time averaged density, as $\Delta n_e = (< n_e >_{cycle} - n_e)$, where $<$

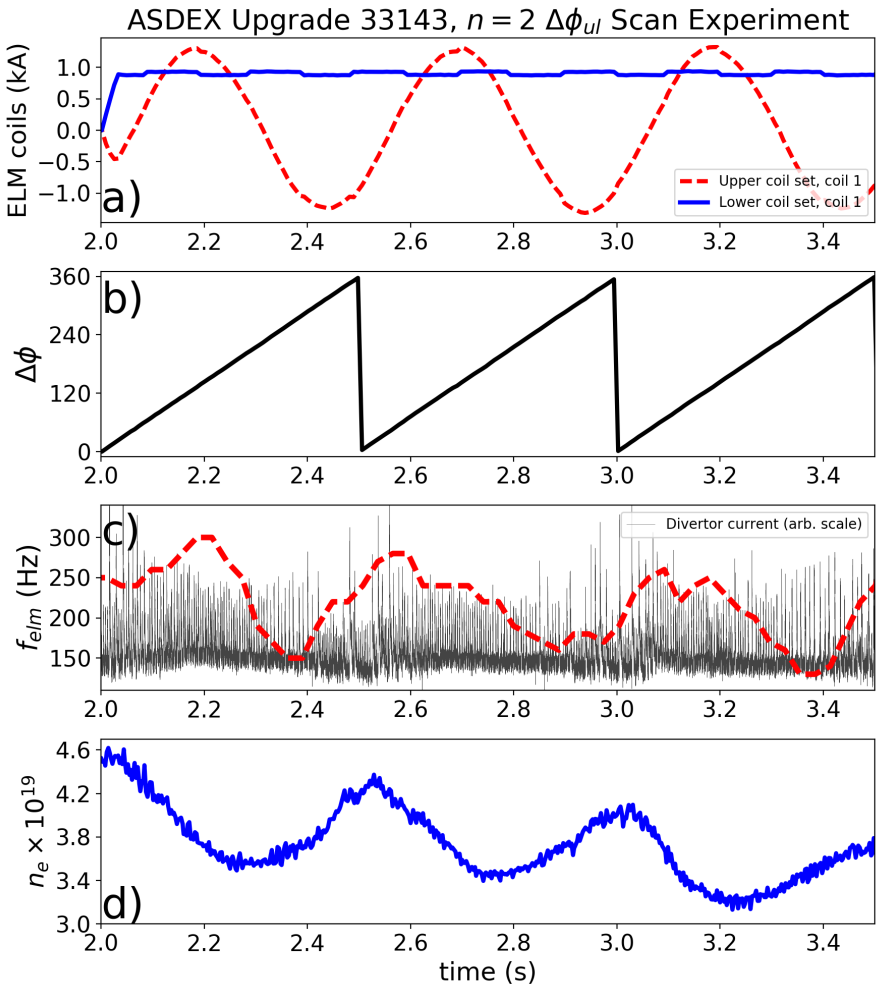

Figure 1. a) A travelling toroidal waveform is applied in the upper coils, while the lower coils are held fixed. b) Thereby, the phase difference between the upper and lower coils $\Delta\Phi_{ul}$ is scanned. c) ELMs manifest as spikes in the divertor current trace (grey). The ELM frequency is computed by counting these spikes (red), and is seen to vary with $\Delta\Phi_{ul}$. d) The line averaged electron density also varies with $\Delta\Phi_{ul}$.

$n_e >_{cycle}$ is the electron density time averaged over a $\Delta\Phi_{ul}$ cycle. The ELM frequency f_{ELM} is calculated by counting ELMs, manifesting as peaks in the divertor current trace, in a moving 100ms window. The moving window was reduced the 20ms to accommodate the faster scan speeds of the $n = 1$ discharges. In this context the notation $\widehat{X} = (X - X_{min})/X_{max}$, such that $\widehat{X}$ takes values from $0 \rightarrow 1$. Using f_{ELM} and Δn_e as X, and their maximum and minimum values in each cycle for X_{min} and X_{max}, f_{ELM} and Δn_e are then normalised to $\widehat{f_{ELM}}$ and $\widehat{\Delta n_e}$. Using the trace of $\Delta\Phi_{ul}(t)$, $\widehat{f_{ELM}(t)}$ and $\widehat{\Delta n_e(t)}$ are mapped from the time domain to the $\Delta\Phi_{ul}$ domain. A function $|(1+exp\{i(\Delta\Phi_{ul}+\Delta\Phi_{opt})\})|/2$ is then fitted to each normalised $\widehat{f_{elm}(\Delta\Phi_{ul})}$ and $\widehat{\Delta n_e(\Delta\Phi_{ul})}$ to determine $\Delta\Phi_{opt,ne}$ and $\Delta\Phi_{opt,ELM}$. This fitting function is chosen because it matches the functional form of $|b^1_{res}|(\Delta\Phi_{ul})$, with which the ELM frequency and density pump out are strongly correlated, and which is therefore used for the numerical optimisation of coil phase. Examples of this procedure, using ASDEX Upgrade discharges

n	Shot	$\Delta\Phi_{ul}$ cycles	B_t	I_p	q_{95}	$n_e \times 10^{19} m^{-3}$	Scan freq. (Hz)
1	31023	4	2.58	1.00	4.36	7.12	2
1	31034	3	2.59	1.00	4.31	7.66	4
1	32100	4	2.49	0.80	5.27	4.82	-10
1	32116	5	2.48	0.80	5.26	5.11	-2
2	30680	5	2.48	0.80	5.24	8.44	2
2	30681	6	2.47	0.80	5.43	6.34	2
2	30682	2	1.77	0.80	3.66	5.20	2
2	30684	5	2.47	0.80	5.17	6.31	1
2	30824	2	2.49	0.80	5.41	5.95	-0.7
2	30826	2	1.79	0.80	3.67	5.65	-0.5
2	31542	2	2.43	0.80	4.99	5.34	0.7
2	31543	2	2.44	0.80	4.99	5.40	0.7
2	31545	2	2.43	0.80	4.99	5.51	0.7
2	33143	3	1.82	0.80	3.84	5.02	2

Table 2. List of ASDEX Upgrade discharges in which the experimental optimal coil phase is measured. $\Delta\Phi_{ul}$ 'cycles' refers to the number of complete rotations of coil phase which are used in this study (in general, a small subset of the total number of complete $\Delta\Phi_{ul}$ rotations)

33143 and 30680, are shown in figures 2 and 3. The latter demonstrates a large scatter in the measured values of $\Delta\Phi_{opt}$. In order to compute the mean and variance of the measurements, $\Delta\Phi_{opt}$ is approximated to be constant throughout the flattop of each shot, so $\Delta\Phi_{ul}$ cycles may be treated as repeated measurements. It is acknowledged that for several discharges only 2 or 3 cycles are available, in which case the mean and standard deviation do not have meaning in the statistical sense. However they are used in the absence of alternatives to express the value and spread of the data. Since the measured data are angular, the mean angular direction and circular standard deviation are used as detailed in[24].

ASDEX Upgrade has two Passive Stabilisation Loops (PSLs) - large copper rings installed above and below the mid plane directly in front of the ELM coils, which enhance vertical stability. Time varying RMP fields are both attenuated and delayed by the PSLs before reaching the plasma. When extracting $\Delta\Phi_{opt}$ from the experimental measurement, the time lag in $\Delta\Phi_{ul}$ caused by the PSLs must be accounted for. For this purpose, a previously developed finite element modelling code[25] is used which shows good agreement with the measured response in [26], to calculate the PSL induced lag for each discharge. Figure 4 shows the computed $\Delta\Phi_{ul}$ both including and neglecting the PSL lag. It is found that for $\Delta\Phi_{ul}$ scans of 2 Hz or higher the PSL induced phase lag was 32 degrees, while a scan at 1 Hz corresponded to a lag of 25 degrees. The direction in which $\Delta\Phi_{ul}$ is scanned (ie, increasing or decreasing) determines whether the lag is added to or subtracted from the measured $\Delta\Phi_{opt}$.

Figure 5 plots the measured phases at which ELM mitigation and density pump out are maximised (corrected for PSL lag), for all cycles and shots studied (crosses and squares

respectively). For the $n = 1$ discharges, no RMP induced modulation in n_e was detected during the $\Delta\Phi_{ul}$ scans, and they are therefore excluded from the plot. The $n = 2$ discharges exhibit a significant offset between $\Delta\Phi_{opt,ne}$ and $\Delta\Phi_{opt,ELM}$, which is evident in the histogram of Figure 5b). On average the optimum coil phase for ELM mitigation is 59.0±60.6 degrees lower than for maximum density pump out. Given the observed correlation between density pump out and ξ_X[17], and also that recent computational works[18] have found that $|b^1_{res}|$ and ξ_X are synchronised as a function of $\Delta\Phi_{ul}$, current theory would lead us to expect no offset between $\Delta\Phi_{opt,ne}$ and $\Delta\Phi_{opt,ELM}$, in contrast to what is experimentally observed here. The discharges used in this study are roughly grouped according to $\Delta\Phi_{ul}$ scan speed and direction, and the separate groups of -0.7 or -0.5 Hz, 0.5 or 0.7 Hz, and 2 Hz are plotted in the histogram in 5b), as blue, green and red lines respectively. The resulting histogram shows that the group of faster rotation speeds have on average a higher shift between $\Delta\Phi_{opt,ne}$ and $\Delta\Phi_{opt,ELM}$, suggesting that the shift is dependent on rotation speed. It is also noted that the size of the shift in the time domain is of the same order as the particle confinement time. These observations suggest that the probable explanation for the shift is the slow timescale of the density response compared with the more immediate response of the ELM frequency. Therefore for the case of a static or rigidly rotating applied field, we would not expect to observe this shift between $\Delta\Phi_{opt,ne}$ and $\Delta\Phi_{opt,ELM}$, in line with current theoretical expectations. Correcting the $\Delta\Phi_{opt,ne}$ measurement to account for the particle transport time in order to determine categorically whether the shift between $\Delta\Phi_{opt,ne}$ and $\Delta\Phi_{opt,ELM}$ is due to the time delay between the density and ELM frequency response, is beyond the scope of this study and not attempted here. The random uncertainty in the experimentally measured $\Delta\Phi_{opt,ELM}$ and $\Delta\Phi_{opt,ne}$ is typically quite high, as plotted in figure 5c) (again including $n = 2$ discharges only), and generally lower for $\Delta\Phi_{opt,ne}$. The uncertainty may be reduced by increasing the sample size (number of cycles) for each discharge.

In order to obtain a rough estimate of the increase in ELM mitigation which may be expected by careful phase alignment of the coils relative to poor or random alignment, the maximum mitigated ELM frequency for each $\Delta\Phi_{ul}$ scan of each discharge is compared with the average ELM frequency over that scan (representing random alignment), and also the minimum ELM frequency over that scan (representing poor alignment). Poor alignment is defined here as $\Delta\Phi_{opt}$+180, where $\Delta\Phi_{opt}$ is the coil phase at which ELM mitigation is maximised. Similarly, to estimate the penalty in density which optimal alignment is expected to cause relative to random or poor alignment, the maximum density pump out (negative density) for each scan is compared with the average and minimum density pump out. Figure 6a) plots (in blue) the maximum negative density normalised to the mean negative density over each scan, against maximum mitigated ELM frequency normalised to the mean ELM frequency over each scan. These figures correspond to the ELM mitigation and density pump out of optimal coil alignment relative to random coil alignment. This comparison relies on the assumption that the density pump out and mitigated ELM frequency are maximised at the same $\Delta\Phi_{ul}$, which despite the shift observed in figure 5 is still expected to be true for static or slowly varying RMPs. Also plotted (in red) is the maximum pump out normalised to the

minimum pump out over each scan, against maximum mitigated ELM frequency normalised to the minimum ELM frequency over each scan. In this plot, outliers in the normalised ELM frequency caused by small or zero measurements of the minimum ELM frequency are discarded, since they are caused by the finite width of the frequency measurement time window. These figures correspond to the ELM mitigation and density pump out of optimal coil alignment relative to poor coil alignment. The figures demonstrate that as well as the known correlation between density pump out and mitigated ELM frequency as a function of $\Delta\Phi_{ul}$, the correlation also holds for maximal ELM mitigation and density pump out between $\Delta\Phi_{ul}$ scans and between discharges. As demonstrated in the histograms in figure 6, the average increase in mitigated ELM frequency caused by optimal coil alignment, relative to random or poor coil alignment, are factors of 1.30$\pm$0.13 and 1.96$\pm$0.55 respectively. The associated decrease in density due to optimal coil alignment relative to random or poor coil alignment, are factors of 0.91$\pm$0.04 and 0.82$\pm$0.07 respectively (ie, optimal alignment has lower density than poor alignment by a factor of approximately 0.82). Due to the small sample size, these figures are representative only of this small survey and for illustrative purposes only; they are not claimed to be representative of general ASDEX Upgrade RMP experiments. It should be noted that since both f_{ELM} and density pumpout are modulated by the externally imposed coil phase, it is not possible to use these experiments to search for causal relationships between density pump out and f_{ELM}, since the modulations of both are driven by an external forcing factor (the coil phase scan). More rigorous investigations of possible dependencies between the density, density pump out and mitigated ELM frequency are reported in other works[36, 15, 37], but are outside the scope of this study.

Since ELM mitigation is the focus of this work, hereafter the mitigated ELM frequency f_{ELM} and not density pump out is used to determine the experimental value of $\Delta\Phi_{opt}$ (ie, hereafter in experimental context $\Delta\Phi_{opt} = \Delta\Phi_{opt,ELM}$).

2.3. Comparison of measured $\Delta\Phi_{opt}$ with predictions

In this section, the experimental measurements of $\Delta\Phi_{opt}$ of the previous section, are compared with the predictions of rigorous MARS-F calculations, and also the previously derived[22] 2D quadratic parametrisation. For each cycle studied of each discharge, the midpoint in time of the cycle is chosen to represent the cycle. At these representative points, $\Delta\Phi_{opt}$ as defined using b^1_{res} is computed with a MARS-F computation as described in [22], using as input CLISTE based equilibria downloaded from the ASDEX Upgrade database, and fitted experimental profiles of T_e, T_i, n_e, and bulk toroidal rotation v_t. Furthermore, $\Delta\Phi_{opt}$ is computed using the 2D quadratic parametrisation, using the values of β_N and q_{95} at the cycle midpoints as input. In figure 7, the experimentally measured $\Delta\Phi_{opt,ELM}$ is plotted against $\Delta\Phi_{opt}$ predicted by MARS-F computations and the 2D quadratic, for $n = 1$ and $n = 2$ discharges. In the $n = 2$ case, the predictions of MARS-F and the 2D quadratic are shown to match the experimental value to within the uncertainty of the measurement. The agreement is

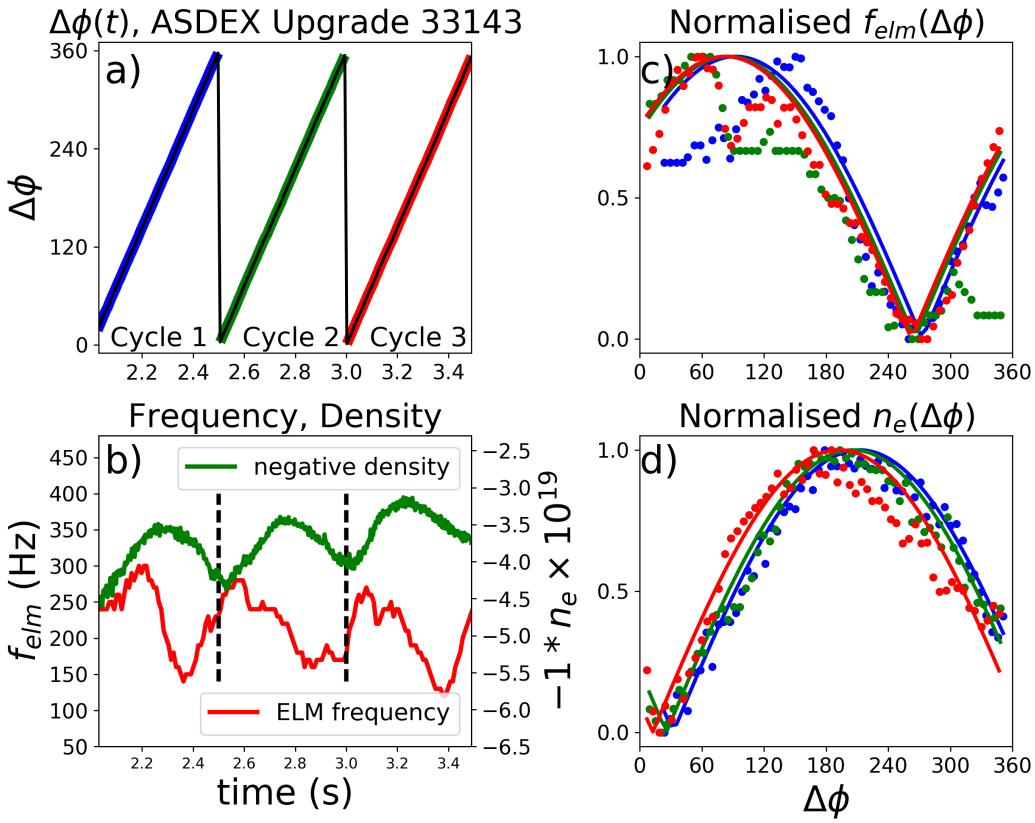

Figure 2. a) $\Delta\Phi_{ul}$ is divided into $0 \rightarrow 2\pi$ cycles. b) The density pump out and mitigated ELM frequency traces are mapped from the time domain to $\Delta\Phi_{ul}$ for each cycle. To display density pump out, the density here is multiplied by -1. c,d) Each cycle of f_{elm} and density pump out is normalised to its maximum and minimum value in that cycle (dots), and the optimum extracted by fitting a $|(1 + exp\{i(\Delta\Phi_{ul} + \Delta\Phi_{opt})\})|/2$ function (solid lines).

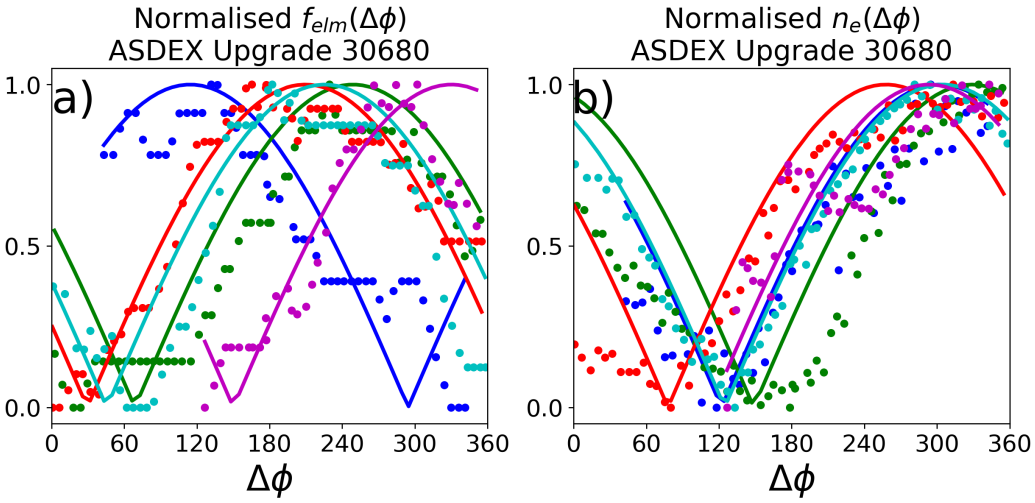

Figure 3. A repeat of figure 2 using shot 30680, demonstrating scatter in the $\Delta\Phi_{opt}$ measurements between cycles for a given shot. Uncertainties are quantified by treating each cycle in a shot as a repeat measurement, to define an average and standard deviation for that shot.

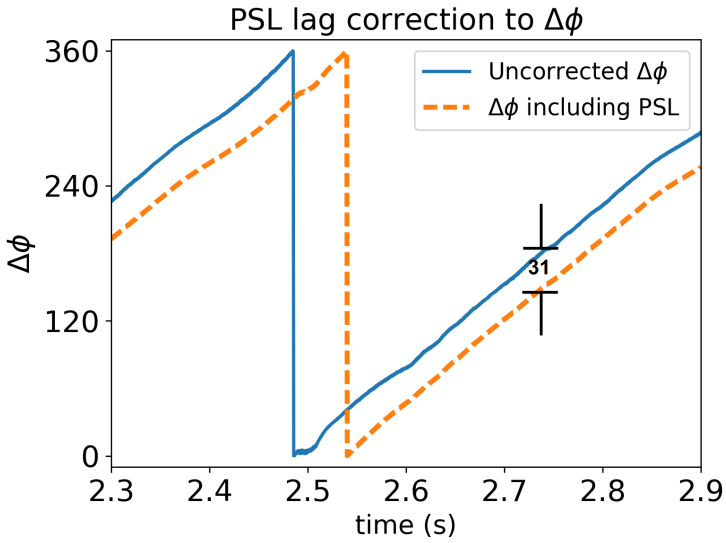

Figure 4. Time varying RMPs induce eddy currents in the Passive Stabilisation Loops, causing the value of $\Delta\Phi_{ul}$ as seen by the plasma to lag behind the value at the ELM coils. Plot created using the code developed in [26].

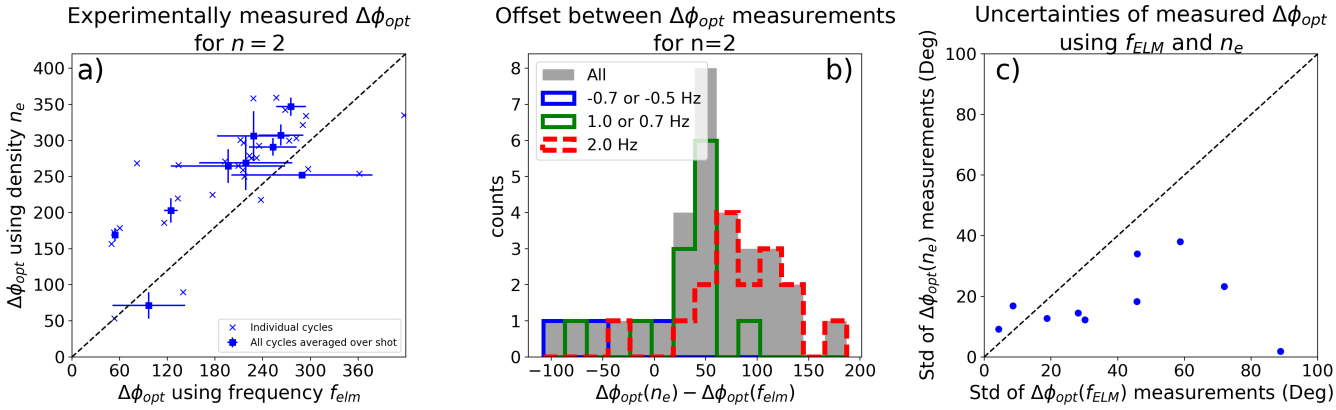

Figure 5. a) $\Delta\Phi_{opt,ne}$ (maximum density pump out) plotted against $\Delta\Phi_{opt,ELM}$ (maximum ELM mitigation). Although $\Delta\Phi_{opt,ELM}$ was measured for $n = 1$ discharge as shown in figure 7, only $n = 2$ shots are included in this plot due to lack of measurable $\Delta\Phi_{opt,ne}$ for $n = 1$ discharges. b) Histogram of $(\Delta\Phi_{opt,ne} - \Delta\Phi_{opt,ELM})$. Current theory leads us to expect no shift between the two optimal phases. However, although the scatter is wide, it appears that $\Delta\Phi_{opt,ne}$ is shifted upwards relative to $\Delta\Phi_{opt,ELM}$. c) Uncertainty in $\Delta\Phi_{opt,ELM}$ and $\Delta\Phi_{opt,ne}$ measurements, computed by assuming the true value is constant for each discharge, and taking a standard deviation of multiple cycles in each discharge. The uncertainties in $\Delta\Phi_{opt,ELM}$ tend to be larger than those of $\Delta\Phi_{opt,ne}$.

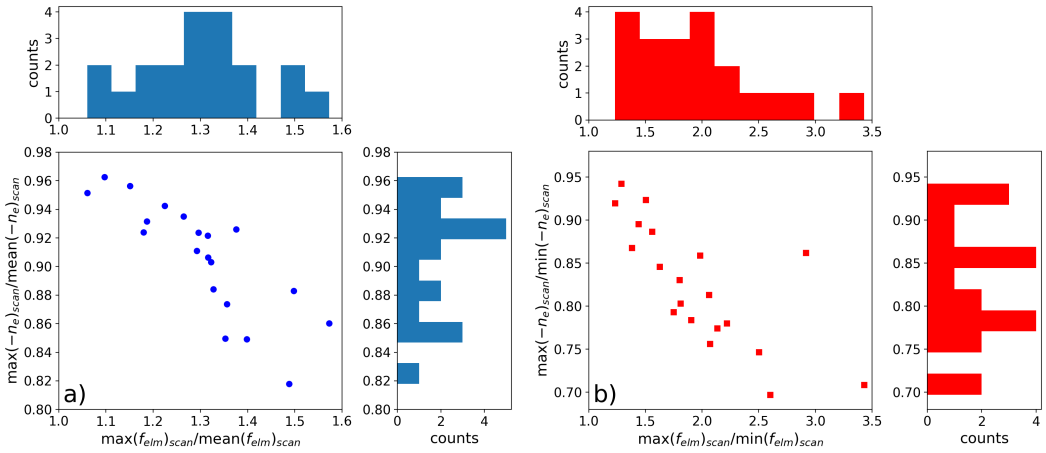

Figure 6. a) For each cycle of $\Delta\Phi_{ul}$ in all $n = 2$ discharges studied, the maximum ELM frequency and density pump out is plotted, normalised to the mean ELM frequency and density pump out over each cycle. b) The maximum ELM mitigation and density pump out is plotted, normalised to the minimum ELM frequency and density pump out over each cycle. Both plots indicate that the maximum ELM mitigation over $\Delta\Phi_{ul}$ scan, is correlated with the maximum pump out over the scan, as expected.

worse for the $n = 1$ discharges, a problem which is compounded by the very small sample size of $n = 1$ discharges, and their clustering in a relatively small range of $\Delta\Phi_{opt}$. The small $n = 1$ error field present on ASDEX Upgrade may cause further error in the $\Delta\Phi_{opt}$ measurements, however rigorously quantifying these errors is outside the scope of this report.

To quantify the comparison between prediction and measurement, an RMSE between the experimental measurements and MARS-F or 2D quadratic predictions is defined as

$$RMSE_{quad} = \left(\sum_{i}^{N} (\Delta\Phi^{i}_{opt,quad} - \Delta\Phi^{i}_{opt,exp})^2 / N \right)^{\frac{1}{2}} \tag{2}$$

$$RMSE_{mars} = \left(\sum_{i}^{N} (\Delta\Phi^{i}_{opt,mars} - \Delta\Phi^{i}_{opt,exp})^2 / N \right)^{\frac{1}{2}} \tag{3}$$

In the above, $\Delta\Phi_{opt,quad}$ is the cycle averaged optimal coil phase for each shot predicted by the 2D quadratic, $\Delta\Phi_{opt,mars}$ is the cycle averaged optimal coil phase for each shot predicted by MARS-F, and $\Delta\Phi_{opt,exp}$ is the cycle averaged experimentally measured $\Delta\Phi_{opt,ELM}$ for each shot. 'Cycle averaged' denotes an (angular) average taken over all studied cycles for a given discharge. It is not claimed that the above definition is statistically robust: the primary use of these RMSE definitions is for a self consistent comparison with the benchmark between the quadratic and MARS-F reported in [22], and do not take account of the uncertainties of the experimental measurement. The RMSEs are calculated for $n = 1$ and $n = 2$ separately. For $n = 1$, the values are found to be $RMSE_{quad} = 55.7$

and $RMSE_{mars} = 46.0$. For $n = 2$, the values are found to be $RMSE_{quad} = 32.1$ and $RMSE_{mars} = 29.6$. The $n = 2$ RMSE values are sufficiently low to allow this parametrisation to be useful in predicting the optimum coil phase for ELM mitigation, however the $n = 1$ RMSE values should be reduced by increasing the number and q_{95} range of $n = 1$ discharges studied.

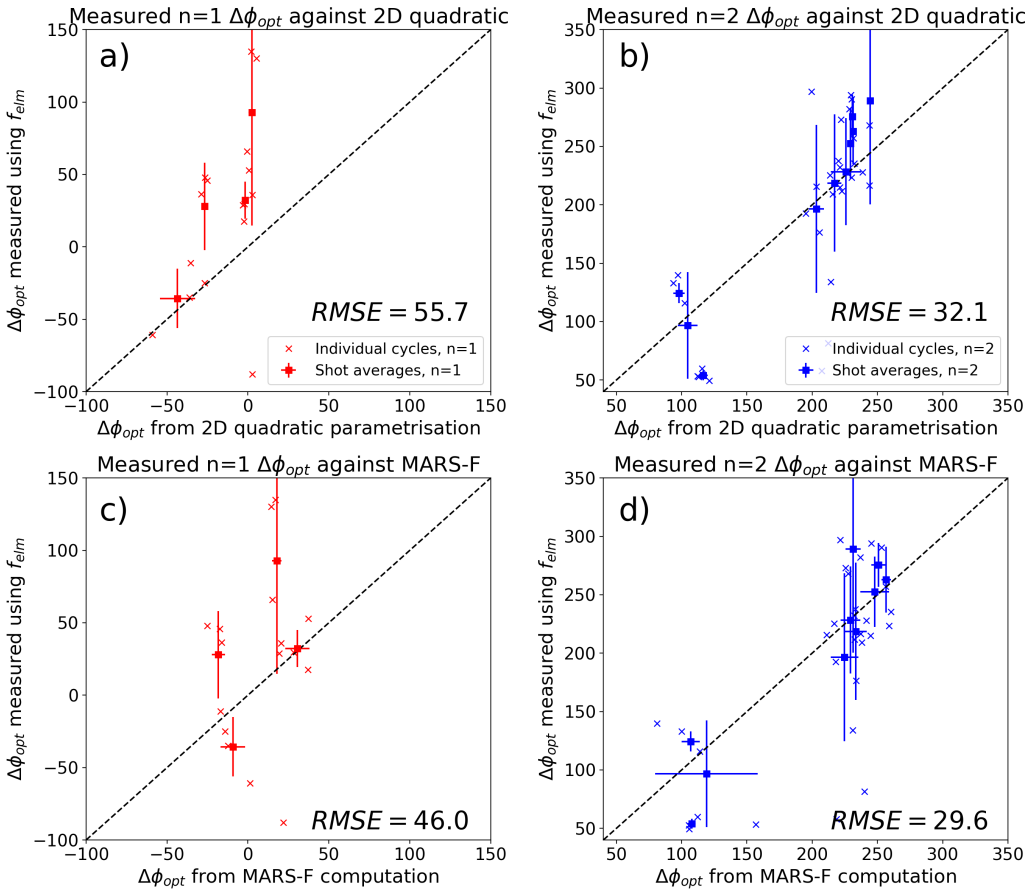

Figure 7. a) $\Delta\Phi_{opt}$ for the $n = 1$ discharges measured from the f_{elm} trace compared with $\Delta\Phi_{opt}$ predicted with the 2D quadratic parametrisation. b) $\Delta\Phi_{opt}$ for the $n = 2$ discharges measured from the f_{elm} trace compared with $\Delta\Phi_{opt}$ predicted with the 2D quadratic parametrisation. c) $\Delta\Phi_{opt}$ for the $n = 1$ discharges measured from the f_{elm} trace compared with $\Delta\Phi_{opt}$ predicted with a MARS-F plasma response computation. d) $\Delta\Phi_{opt}$ for the $n = 2$ discharges measured from the f_{elm} trace compared with $\Delta\Phi_{opt}$ predicted with a MARS-F plasma response computation.

3. Choice of Toroidal Waveform

This report and others [22, 18] focus primarily on optimisation of $|b^1_{res}|$ by tuning the coil phase difference $\Delta\Phi_{ul}$. The optimum coil phase may take any arbitrary value depending on equilibrium parameters, and therefore precise alignment requires a sinusoidal toroidal waveform which can take any arbitrary phase. However, producing a sinusoidal waveform

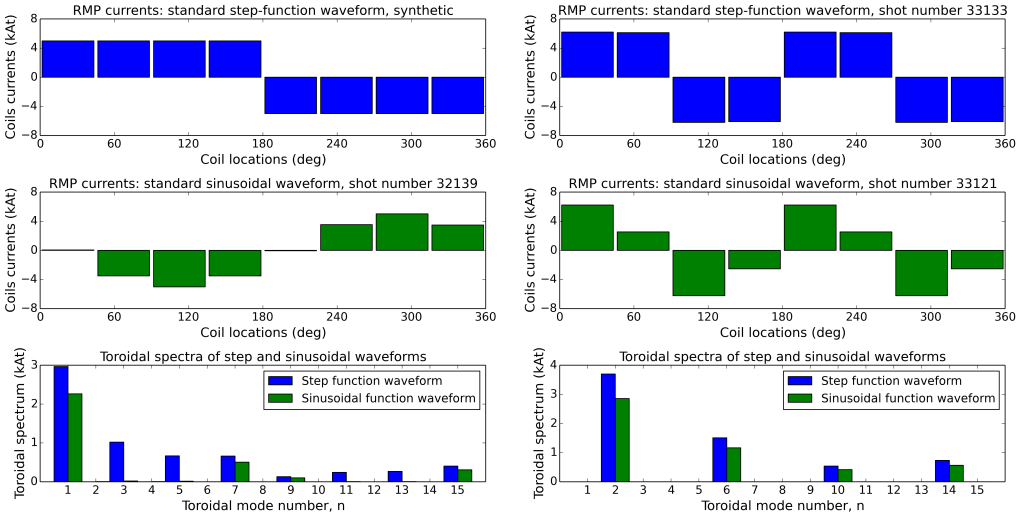

Figure 8. Choosing either a sinusoidal or rectangular toroidal current waveform, presents a trade off between flexibility and amplitude.

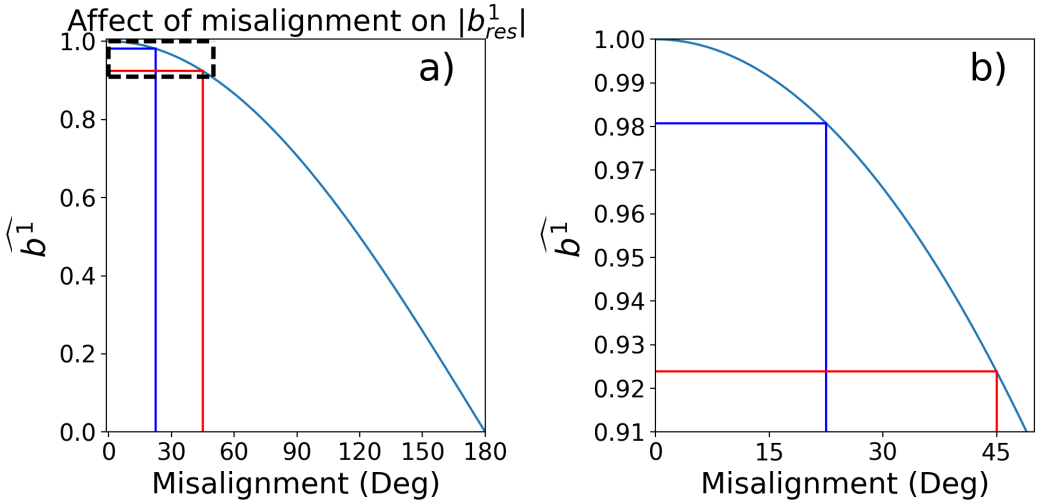

Figure 9. a) $\widehat{b^1}$ represents the maximum penalty which may be incurred to b^1_{res} due to coil phase misalignment. Since the function has zero gradient at perfect alignment, small misalignments result in only minor penalties in amplitude, making rectangular waveforms viable for ELM control. b) Plot magnified to the dashed rectangle in a).

necessitates most of the RMP coils to carry less than their maximum current capacity, as demonstrated in figure 8. The figure compares the toroidal waveform of a rectangular RMP toroidal waveform with a sinusoidal waveform, both with the same maximum amplitude, and plots the resulting toroidal spectrum of each. The sinusoidal toroidal waveform more closely adheres to a true $n = 1, 2$ sinusoid, and therefore has lower toroidal sidebands compared with the rectangular waveform, but also has a lower dominant toroidal component n_{dom} than the rectangular waveform. In the linear approximation (used in the MARS model) a reduction of the n_{dom} component of the applied current causes a corresponding reduction in $|b^1_{res}|$, and

therefore the mitigated ELM frequency. In the $n_{dom} = 1, 2$ cases examined here, the dominant n component of the sinusoidal waveform $n_{dom,sin}$ is approximately 77% of the dominant n component of the rectangular waveform, $n_{dom,rec}$, making rectangular waveforms potentially superior to sinusoids for ELM control.

Conversely, a rectangular waveform may only be tuned to certain discrete values of coil phase, namely, $\Delta\Phi_{ul}$ may take values $j(360 * n/N)$ where $j = 0, 1, 2, (N/n) - 1$. For example an $n = 2$ RMP applied using 8 coils may have $\Delta\Phi_{ul} = 0, 90, 180, ..,$ and an $n = 1$ may have $\Delta\Phi_{ul} = 0, 45, 90, ...$ This introduces an unavoidable misalignment of rectangular RMP waveforms, which (assuming the value of $\Delta\Phi_{ul}$ is chosen which is the closest to optimum alignment) may be as great as $(360 * n/N)/2$, ie, 22.5 degrees for N=8, $n = 1$, or 45 degrees for N=8, $n = 2$. To quantify the maximum reduction in $|b^1_{res}|$ which may be caused by misalignment, a normalised $\widehat{b^1}$ is defined to be unity at optimum alignment and zero at optimum misalignment, ie, $\widehat{b^1}(\Delta\Phi_{opt})$ = 1 and $\widehat{b^1}(\Delta\Phi_{opt} + 180)$ = 0. Figure 9 plots $\widehat{b^1}$ with $\Delta\Phi_{ul}$. As the figure shows, the maximum reduction in $|b^1_{res}|$ of a 22.5 and 45 degree misalignment are factors of 0.98 and 0.92 respectively. In general the reduction will be less severe than this, since the minimum of $|b^1_{res}(\Delta\Phi_{ul})|$ is generally not zero, and also because 22.5 and 45 degrees are the upper bounds of the unavoidable misalignment for $n = 1$ and $n = 2$ fields with $N = 8$, representing the case where the true optimum phase is exactly equidistant between two allowed experimental phases. We now let $b_{opt,sin}$ be b^1_{res} for an optimally aligned sinusoidal waveform, $b_{opt,rect}$ be b^1_{res} for an optimally aligned rectangular waveform, and $b_{mis,rect}$ be b^1_{res} for a 45 degree misaligned rectangular waveform (ie, the worst case misalignment for an $n = 2$ RMP with 8 RMP coils).

It was established in the above that $b_{opt,sin} = 0.77 b_{opt,rect}$, and that $b_{mis,rect} = 0.92 b_{opt,rect}$. Therefore, $b_{opt,sin} = 0.84 b_{mis,rect}$. To rephrase, a 45 degree misaligned rectangular waveform produces a larger $|b^1_{res}|$ than an perfectly aligned sinusoidal waveform with the same maximum coil current. It follows from simple symmetry considerations that $b_{opt,sin}/b_{opt,rect}$ is approximately independent of n and N and therefore fixed at around 77%. However the ratio $b_{mis,rect}/b_{opt,rect}$ does depend on n and N, since it depends on the degree of unavoidable misalignment which is bounded above by $(360 * n/N)/2$. Reading from figure 14, the misalignment required to cause this same reduction is 80 degrees. From this we can deduce that the reduction in $|b^1_{res}|$ due to unavoidable misalignment of a rectangular waveform will always be less than the reduction due to the use of a sinusoidal waveform for applied fields which satisfy $(360 * n/N)/2 < 80$, ie, $n/N < 4/9$. Although this criteria is derived using an $N = 8$ coil set for illustration, as explained above the criteria is general for any N or n, including the $N = 9$ coil set of ITER. It should be noted however, that the case of an $n = 4$ field applied using the ITER coil set does not strictly satisfy the $n/N < 4/9$ criteria, but is a marginal case.

Sinusoidal waveforms have the advantage that they may be precisely aligned such that $\Delta\Phi_{ul} = \Delta\Phi_{opt}$, however the required reduction in total coil current compared with a 'minimally misaligned' rectangular waveform more than compensates for this, if the condition

$n/N < 4/9$ is satisfied. Therefore, a rectangular toroidal waveform satisfying $n/N < 4/9$ would be expected to induce superior ELM mitigation compared with a sinusoidal waveform, despite not being able to achieve perfect alignment. However, other concerns may rule out rectangular waveforms. For example, a recent computational study of RMP induced plasma deformation in ITER, has indicated that beating between the main toroidal harmonic and sidebands may cause toroidal localisation of the heat deposition profile[27]. Since rectangular waveforms have much larger sidebands relative to sinusoidal waveforms, it is expected that this toroidal heat load localisation may be ameliorated by the use of sinusoidal toroidal waveforms. Unintentional sidebands of rectangular waveforms may also complicate interpretations of experimental results by having dependencies on coil phase which differ from the dominant toroidal mode number. They may also cause currents to be driven at additional rational surfaces, increasing $j \times b$ braking of the plasma rotation, which is often undesirable.

4. ITER Coil Phase Parametrisation

Effective active ELM mitigation will be required in the ITER tokamak at all times during a discharge, even the current and pressure ramp[14]. During the ramp, the optimal coil alignment will be altered considerably by the changes to q_{95} and β_N. It may therefore be necessary to actively track the optimal alignment to maintain an acceptable level of ELM mitigation. To this end, in this section the optimal coil phase for ITER is parametrised using the previously developed technique reported and benchmarked in [22], and validated in section 2 of this work.

The ITER ELM control coil set will consist of an upper, mid plane and lower set, sketched in figure 10. The principle of superposition is used to add the RMP fields due to the upper, middle and lower coils as in [22], with the minor change that the field is now the linear sum of three sets of coils instead of two. The mid plane coil set is held fixed and the upper and lower sets rotated, such that the field due to all three coils b_{UML} is

$$b_{UML} = b_M + b_U exp\{-i\Delta\Phi_{UM}\} + b_L exp\{-i\Delta\Phi_{LM}\} \tag{4}$$

where b_M, b_U and b_L are the fields due to the mid plane, upper and lower coil sets respectively. $\Delta\Phi_{UM}$, $\Delta\Phi_{LM}$ are the coil phase differences between the mid plane coil set and the upper and lower coils respectively, defined as $\Delta\Phi_{UM} = \Delta\Phi_M - \Delta\Phi_U$, $\Delta\Phi_{LM} = \Delta\Phi_M - \Delta\Phi_L$, where $\Delta\Phi_U$, $\Delta\Phi_M$, $\Delta\Phi_L$, are the phases of the coil current toroidal waveforms of the upper, mid plane and lower coils. The optimal upper and lower coil phases, defined as the upper and lower coil phases which maximise $|b^1_{res}|$, are denoted here as $\Delta\Phi_{opt,UM}$ and $\Delta\Phi_{opt,LM}$.

As explained in [22], the pitch aligned component due to the three coils is optimised when both $b^1_{res,U}$ and $b^1_{res,L}$ are parallel to $b^1_{res,M}$ in the complex plane. Therefore, $\Delta\Phi_{UM,opt}$

and $\Delta\Phi_{LM,opt}$ both have unique values for a given equilibrium and perturbation, which may be found simply as

$$\Delta\Phi_{UM,opt} = \pm\, arccos\left(\frac{b^{1,m}_{res}\cdot b^{1,u}_{res}}{|b^{1,m}_{res}||b^{1,u}_{res}|}\right) \tag{5}$$

$$\Delta\Phi_{LM,opt} = \pm\, arccos\left(\frac{b^{1,m}_{res}\cdot b^{1,l}_{res}}{|b^{1,m}_{res}||b^{1,l}_{res}|}\right) \tag{6}$$

where $b^{1,u}_{res}$, $b^{1,m}_{res}$ and $b^{1,l}_{res}$ are the outermost pitch aligned components due to the upper, mid plane and lower coils. The pitch aligned component b^{1}_{res} due to the summed upper, mid plane and lower coils with varying $\Delta\Phi_{UM}$ and $\Delta\Phi_{LM}$, is plotted in figure 11. The plot also includes the values of $\Delta\Phi_{UM,opt}$ and $\Delta\Phi_{LM,opt}$ as given by equations (5) and (6). The figure demonstrates that the formulae match the scan results, making 2D scans in ($\Delta\Phi_{UM}$, $\Delta\Phi_{LM}$) space redundant. This result also demonstrates that the optimal phases are independent of the amplitudes of $b^{1,u}_{res}$, $b^{1,m}_{res}$ and $b^{1,l}_{res}$, and are therefore independent of the amplitude of the current waveforms in each coil row. The sign uncertainty in equations 5 and 6 is resolved by simply choosing the sign which results in the larger amplitude of $|b^{1}_{res}|$.

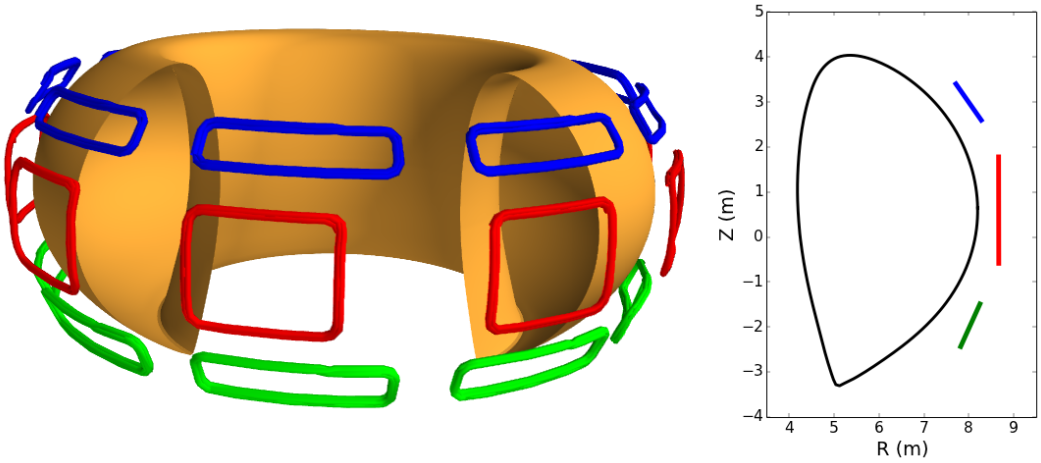

Figure 10. ITER will have 3 rows of 9 coils each installed, an upper, lower and mid plane row. Therefore both the phase between the middle and upper coils $\Delta\Phi_{UM}$, and between the middle and lower coils $\Delta\Phi_{LM}$, may be varied.

4.1. ITER reference equilibrium and scaled equilibrium set

To derive a 2D parametrisation of the optimal coil phase for ITER, a reference equilibrium was scaled in plasma pressure and current using the CHEASE code[28], to produce a set of self consistent equilibria, spanning a wide range of (q_{95}, β_N). The equilibrium set, as well as three example equilibrium profiles, are plotted in figure 12. Coil alignment is determined

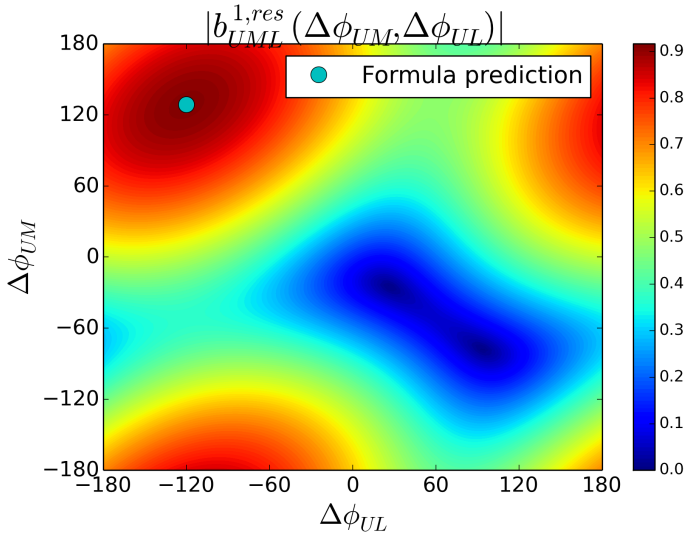

Figure 11. b^1_{res} plotted as a function of $\Delta\Phi_{UM}$ and $\Delta\Phi_{LM}$, as well as the location of ($\Delta\Phi_{UM,opt}$, $\Delta\Phi_{LM,opt}$) predicted using formulae 5 and 6.

primarily by the pressure and safety factor profiles close to the plasma edge. In this study the former is varied by scaling β_N, and the latter by rigidly shifting the q profile by scaling the plasma current. Therefore the total plasma current is allowed to take unrealistically high values, in order to lower q_{95} without modifying q'. The synthetic reference equilibrium used here represents the standard ELMy H-mode scenario for 15MA Q=10 discharges[29, 30], as used in previous works[31, 32, 33], originally produced using the CORSICA code[34]. Figure 13 plots the profiles of the reference equilibrium. The original plasma rotation profile included a sharp decrease to zero at the plasma edge. Recent works have indicated that a zero crossing in the rotation can drastically alter the plasma response locally[35]. In this study the rotation profile is modified to be finite at the edge, in order to avoid a rotation zero crossing being co-located with the outermost resonant surfaces, which would not be the general case and merely obstruct the purpose of this study. In a previous study [22], the optimal coil phase was computed with MARS-F while the rotation profile was scaled by factors ranging from 0.1 to 10. The optimal coil phase was found to be robust to this rotation profile scaling to within 10 degrees. This suggests that the optimal coil phase is robust to changes in the rotation profile (other than the case of there being zero rotation precisely at the plasma edge, which is not studied). Therefore, the parametrisation computed here is not expected to be compromised by uncertainty in the ITER rotation profile.

4.2. Parametrisation of ITER coil phase

The vacuum and total fields due to the applied upper, mid plane and lower RMP coils are computed using MARS-F at each equilibrium point in (q_{95}, β_N) space, for toroidal mode numbers $n = 1 - 4$. From each such computation, the optimal coil phases $\Delta\Phi_{UM,opt}$ and

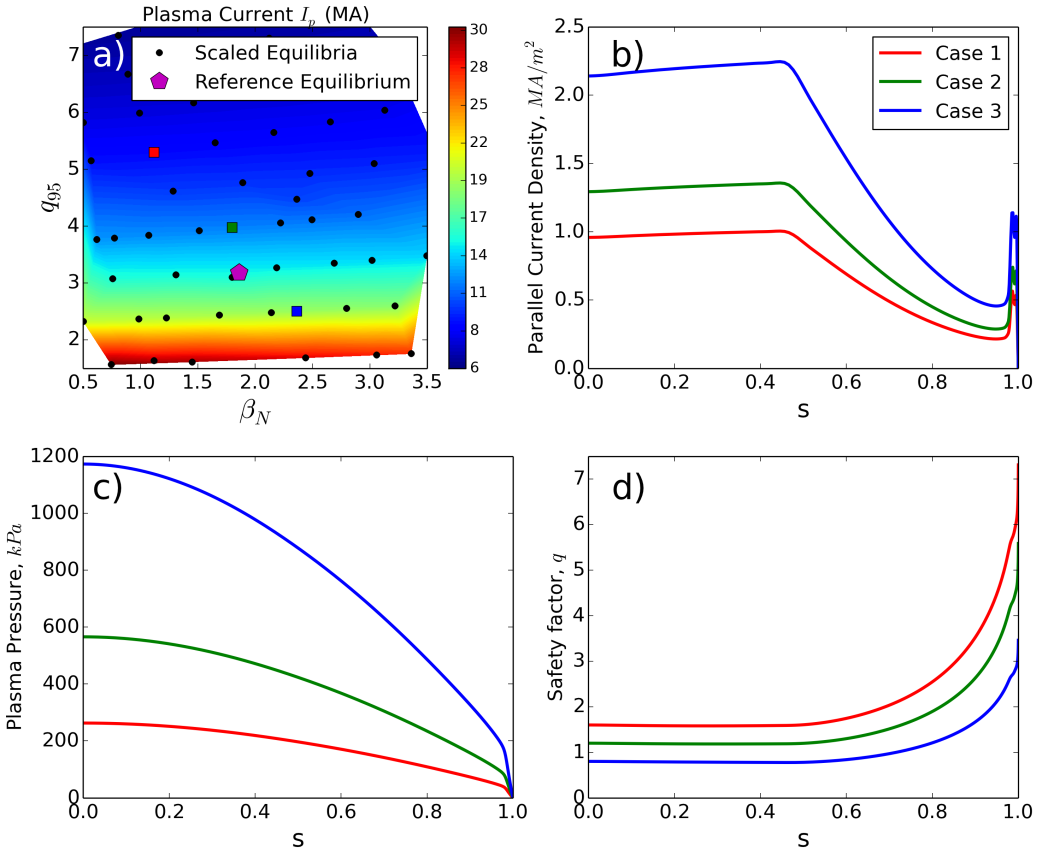

Figure 12. Equilibrium set is produced by scaling a reference equilibrium in current and pressure using CLISTE. a) The set of scaled equilibria, and three example equilibrium points used to demonstrate how the scaling is performed. The black markers plot the simulation points in (q_{95}, β_N) space. For these example points the figure plots b) the plasma current density, c) the plasma pressure and d) the safety factor profile.

$\Delta\Phi_{LM,opt}$ are then extracted with equations 5 and 6. Figure 14 shows the resulting $\Delta\Phi_{UM,opt}$ and $\Delta\Phi_{LM,opt}$ (for the case of $n = 2$), plotted as a function of (q_{95}, β_N). The behaviour matches previous observations[22]: $\Delta\Phi_{LM,opt}$ and $\Delta\Phi_{UL,opt}$ decrease with increasing q_{95} and increase with increasing β_N. $\Delta\Phi_{UM,opt}$ displays the inverse behaviour, which is intuitive when one considers that in the case of $\Delta\Phi_{UL}$ and $\Delta\Phi_{LM}$, the coil which is static is above the coil which is rotated, whereas this is reversed for $\Delta\Phi_{UM}$. This essentially inverts the definition of the coil phase shift, explaining the opposite behaviour with (q_{95}, β_N).

For each of the 8 datasets of optimal coil phases ($n = 1 - 4$, vacuum and total fields), a 2D quadratic function is fitted to the scan for $\Delta\Phi_{UM,opt}$, $\Delta\Phi_{LM,opt}$ and $\Delta\Phi_{UL,opt}$. The form of the quadratic is the same as was used for the ASDEX Upgrade parametrisation, given in equation 1, and the coefficients of the quadratic for $\Delta\Phi_{UM,opt}$, $\Delta\Phi_{LM,opt}$ and $\Delta\Phi_{UL,opt}$ are listed in tables 3, 4 and 5 respectively. The residuals between the MARS-F simulation and the fitted parametrisation for $\Delta\Phi_{UM,opt}$, $\Delta\Phi_{LM,opt}$ and $\Delta\Phi_{UL,opt}$, for the total field with $n = 2$, are plotted in figure 15. The figure shows that the fit generally represents the simulation data to

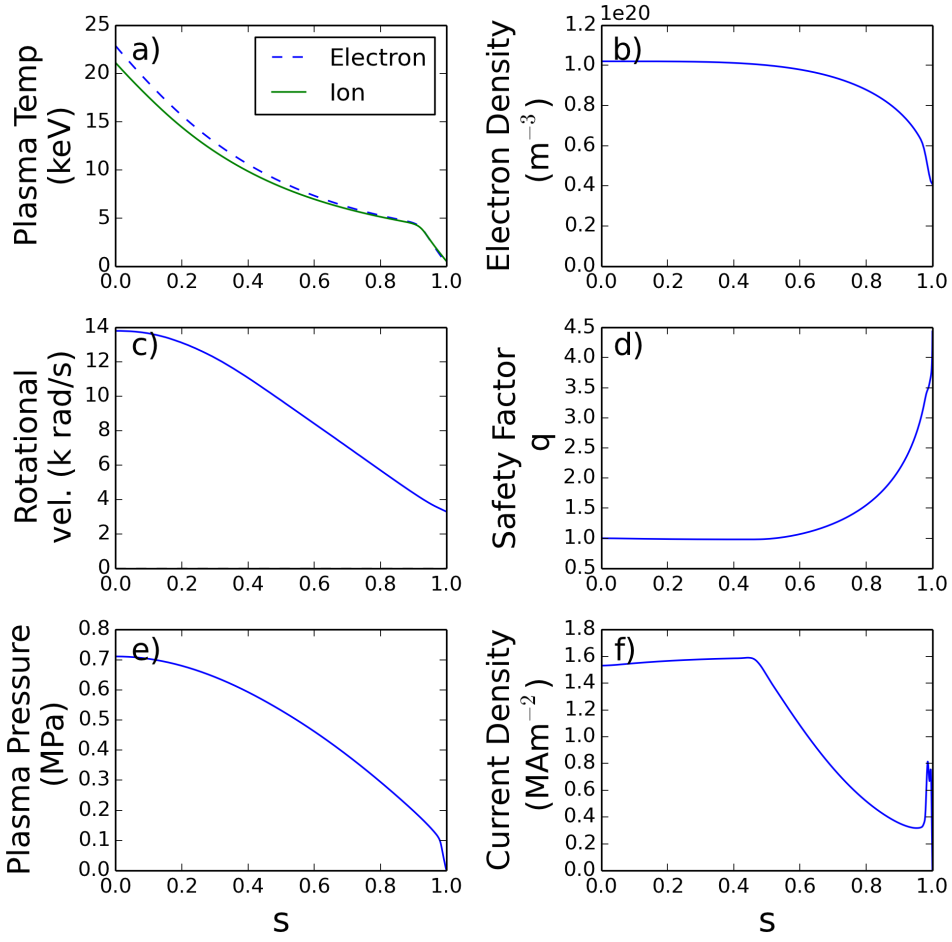

Figure 13. Profiles of the synthetic ITER reference equilibrium used for this study. a) Electron and Ion temperatures. b) Electron number density. c) Plasma bulk rotation velocity. d) Safety factor profile. e) Plasma pressure. f) Plasma current, which is flattened in the core due to the time averaged model of sawteeth used in [30].

within 10 degrees. In a small subset of the points the residuals are slightly larger in magnitude than average. The most likely explanation for these points is that at they have fallen within narrow regions in which there are large resonant field amplification peaks, caused by nq_a being immediately below an integer. This phenomenon is more apparent in the results of [22], which uses a finer grid resolution. In this work as before, these points do not significantly modify the 2D quadratic fit, which is dominated by points outside the resonant peaks.

Currently experimental data from ITER ELM mitigation experiments is unavailable, therefore benchmarking against MARS-F and validation against experiment is not possible for the case of the ITER coil phase parametrisation. However, the successful benchmarking and validation of the same procedure for ELM mitigation in ASDEX Upgrade, reported here and in [22], leads us to expect this ITER parametrisation to have similar accuracy. It is noted however that the parametrisation of the coil phase on ASDEX Upgrade was based on equilibria reconstructed from measurements, whereas the ITER parametrisation is based on

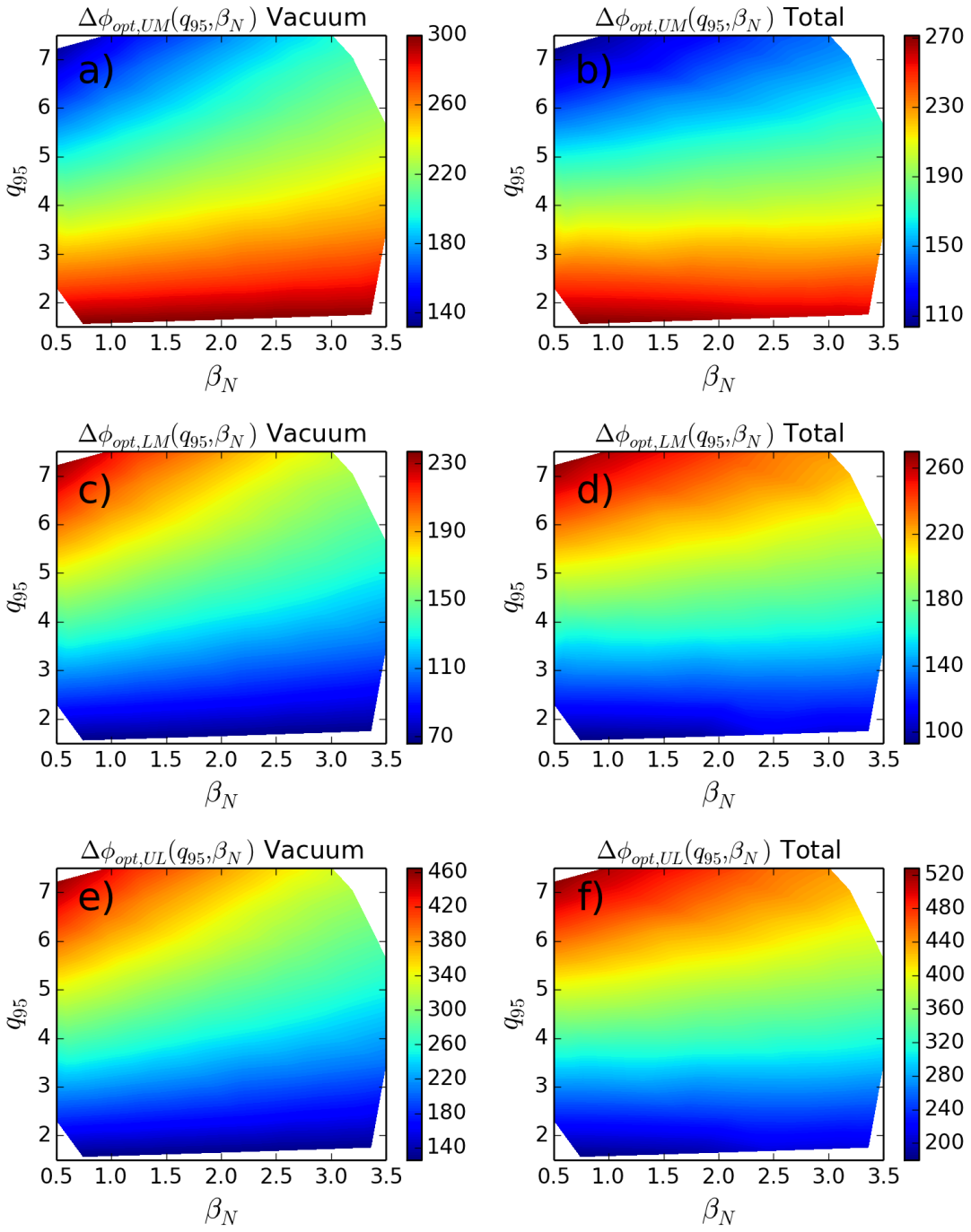

Figure 14. $\Delta\Phi_{UM,opt}$, $\Delta\Phi_{LM,opt}$ and $\Delta\Phi_{UM,opt}$ as a function of (q_{95}, β_N) for $n = 2$. As found in [22], the optimum coil phase is a smoothly varying function of (q_{95}, β_N). These data are the result of MARS-F simulations. When the data are produced, they are wrapped such that they are always between 0 and 360. Since the phase wraps do not have physical significance and merely obscure the underlying trends and complicate curve fitting, they have been removed by adding integer multiples of 360.

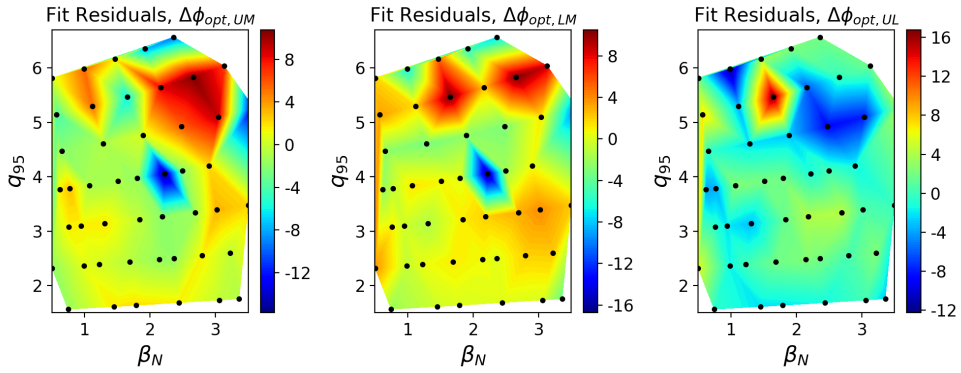

Figure 15. Plot of the residuals between the MARS simulation and parametrisation for $\Delta\Phi_{UM,opt}$, $\Delta\Phi_{LM,opt}$ and $\Delta\Phi_{UM,opt}$, for the field including the plasma response (the total field) and for $n = 2$. Where the residuals are abnormally large, these points are mostly likely caused by resonant field amplification peaks corresponding to nq_a being just below an integer, as explained in [22].

coeff	a	b	c	d	e	f	g	h	i
n=1 vacuum	-0.093339	0.65196	-1.7561	0.56293	-2.6838	9.1661	-0.32757	-11.609	-31.172
n=1 total	-0.030495	0.0022716	0.75543	0.42393	-1.6034	-3.3731	-0.23629	-13.996	-41.55
n=2 vacuum	-0.015844	-0.44548	0.70874	0.20367	4.4907	-6.2807	0.77959	-38.327	355.25
n=2 total	0.015959	-0.48245	1.4953	0.23243	2.7549	-11.035	0.53742	-37.057	333.41
n=3 vacuum	-0.099686	-0.16439	0.71514	0.57838	4.7165	-7.6413	0.88612	-53.879	354.39
n=3 total	-0.080711	0.081354	0.89951	0.71276	1.1883	-9.4082	0.90171	-54.174	334.55
n=4 vacuum	0.42932	-4.239	6.8794	-2.0015	25.825	-38.641	4.4783	-93.381	388.34
n=4 total	0.56781	-4.2563	5.9856	-2.1775	21.225	-33.297	4.5186	-91.101	360.36

Table 3. Coefficients of 2D quadratic parametrisation of $\Delta\Phi_{opt,UM}$ for the ITER ELM coils.

coeff	a	b	c	d	e	f	g	h	i
n=1 vacuum	-0.0040945	0.23158	-0.16038	0.041565	-3.228	4.0099	-1.0093	26.254	-1.4536
n=1 total	-0.13202	1.8511	-6.1309	0.21643	-5.7448	24.184	-0.45666	22.314	23.664
n=2 vacuum	0.0073706	0.70125	-1.4941	-0.18402	-5.5805	9.2475	-0.67467	38.524	9.2087
n=2 total	0.13834	-0.67627	0.18032	-0.74705	0.64012	7.4795	-0.082304	35.022	32.787
n=3 vacuum	0.14185	0.076632	-0.82116	-0.81665	-4.3284	7.9093	-0.56298	54.108	9.3993
n=3 total	-0.11585	1.9406	-5.2864	-0.21655	-7.001	22.22	-0.83178	57.457	22.492
n=4 vacuum	0.45059	-1.6385	1.908	-2.3938	3.0733	-4.9654	0.94217	59.418	28.866
n=4 total	0.18459	-1.6625	3.042	-1.9643	7.9322	-9.5015	0.33647	63.183	43.615

Table 4. Coefficients of 2D quadratic parametrisation of $\Delta\Phi_{opt,LM}$ for the ITER ELM coils.

synthetic equilibria. The extent to which the equilibrium used here as a reference will be representative of general ITER plasmas, represents a currently unquantified uncertainty.

coeff	a	b	c	d	e	f	g	h	i
n=1 vacuum	0.089244	-0.42037	1.5958	-0.52136	-0.54417	-5.1562	-0.68175	37.863	29.719
n=1 total	-0.10153	1.8488	-6.8863	-0.2075	-4.1414	27.557	-0.22037	36.311	-294.79
n=2 vacuum	0.023215	1.1467	-2.2028	-0.38769	-10.071	15.528	-1.4543	76.851	13.963
n=2 total	0.12238	-0.19382	-1.3149	-0.97948	-2.1147	18.514	-0.61972	72.079	-300.62
n=3 vacuum	0.24153	0.24102	-1.5363	-1.395	-9.0449	15.551	-1.4491	107.99	15.012
n=3 total	-0.035142	1.8592	-6.1859	-0.92931	-8.1893	31.628	-1.7335	111.63	-312.06
n=4 vacuum	0.021267	2.6004	-4.9714	-0.39234	-22.751	33.675	-3.5361	152.8	-359.47
n=4 total	-0.38322	2.5938	-2.9437	0.2132	-13.293	23.796	-4.1822	154.28	-316.74

Table 5. Coefficients of 2D quadratic parametrisation of $\Delta\Phi_{opt,UL}$ for the ITER ELM coils.

5. Summary and Conclusions

By gathering experiments from the ASDEX Upgrade database in which $\Delta\Phi_{ul}$ is scanned, $\Delta\Phi_{opt,ELM}$ and $\Delta\Phi_{opt,ne}$ are extracted for 14 discharges, and the uncertainties in the measurement estimated by treating successive sweeps of $\Delta\Phi_{ul}$ as repeat measurements. It was found that $\Delta\Phi_{opt,ne}$ is shifted upwards relative to $\Delta\Phi_{opt,ELM}$ by on average 59.0$\pm$60.6 degrees. It is expected that this shift is due to a lag in the density evolution relative to the ELM frequency which is not accounted for here, and therefore the observed shift is not expected in static or rigidly rotating applied fields. Comparing the mitigated ELM frequency at optimal alignment to the mean and minimum mitigated ELM frequency over all studied $\Delta\Phi_{ul}$ scans, it is found that optimally aligning the RMP increases the mitigated ELM frequency by factors of 1.30$\pm$0.13 and 1.96$\pm$0.55 relative to random or poor alignment respectively. These figures represent a small survey, and are not claimed to be representative of ASDEX Upgrade RMP experiments. By comparing the predictions of $\Delta\Phi_{opt}$ made by the previously derived parametrisation, to experimental measurements of $\Delta\Phi_{opt,ELM}$, it was shown that the parametrisation is sufficient to predict $\Delta\Phi_{opt,ELM}$ to within 32.1 degrees for $n = 2$ discharges. The agreement between experiment and measurement was poor for $n = 1$ discharges, which may be improved by including more $n = 1$ discharges in the study, with a wider range $\Delta\Phi_{opt}$ (requiring a larger range of q_{95}). By comparing $|b^1_{res}|$ due to a perfectly aligned sinusoidal toroidal current waveform, to $|b^1_{res}|$ due to a 'minimally misaligned' rectangular waveform, it is argued that rectangular waveforms should lead to superior ELM mitigation if the condition $n/N < 4/9$ is satisfied. However, sinusoidal waveforms may be required for other reasons, such as to reduce toroidal localisation of the heat deposition profile[27] due to beating between the main toroidal harmonic and sidebands. The 2D quadratic parametrisation was re-derived for the ITER tokamak, using a reference equilibrium representing the standard ELMy H-mode scenario for 15MA Q=10 discharges. The coefficients for $\Delta\Phi_{UM,opt}$, $\Delta\Phi_{LM,opt}$ and $\Delta\Phi_{UL,opt}$ are given here for future use.

Acknowledgements

The careful corrections and insightful suggestions of Dr Hendrik Meyer, Dr Chris Ham and Dr Wolfgang Suttrop are gratefully acknowledged. This work has been carried out within the framework of the EUROfusion Consortium and has received funding from the Euratom research and training programme 2014-2018 under grant agreement No 633053, and is part-funded by the EPSRC through the Fusion Doctoral Training Network (grant number EP/K504178/1), and part-funded by the RCUK Energy Programme (under grant EP/P012450/1). To obtain further information on the data and models underlying this paper please contact PublicationsManager@ukaea.uk. The views and opinions expressed herein do not necessarily reflect those of the European Commission.

References

[1] H. Meyer *et al*, 2017, *Nuclear Fusion*, **57**, 102014.
[2] H. Zohm, 1996, *Plasma Physics and Controlled Fusion*, **38**, 105–128.
[3] A. W. Leonard, 2014, *Physics of Plasmas*, **21**, 090501.
[4] A Loarte *et al*, 2003, *Plasma Physics and Controlled Fusion*, **45**, 1549–1569.
[5] A Kirk *et al*, 2013, *Nuclear Fusion*, **53**, 043007.
[6] B. Sieglin *et al*, 2013, *Plasma Physics and Controlled Fusion*, **55**, 124039.
[7] P T Lang *et al*, 2013, *Nuclear Fusion*, **53**, 043004.
[8] J. C. Vallet *et al*, 1991, *Physical Review Letters*, **67**, 2662–2665.
[9] H. Zohm *et al*, 2015, *Nuclear Fusion*, **55**, 104010.
[10] T E Evans *et al*, 2004, *Physical Review Letters*, **92**, 235003.
[11] Y M Jeon *et al*, 2012, *Physical Review Letters*, **109**, 035004.
[12] Y. Liang *et al*, 2007, *Physical Review Letters*, **98**, 265004.
[13] W Suttrop *et al*, 2011, *Physical Review Letters*, **106**, 225004.
[14] T E Evans, 2013, *Journal of Nuclear Materials*, **438**, S11–S18.
[15] A Kirk *et al*, 2015, *Nuclear Fusion*, **55**, 043011.
[16] A Kirk *et al*, 2013, *Plasma Physics and Controlled Fusion*, **55**, 015006.
[17] Y Liu *et al*, 2011, *Nuclear Fusion*, **51**, 083002.
[18] L Li *et al*, 2016, *Nuclear Fusion*, **56**, 126007.
[19] D A Ryan *et al*, 2015, *Plasma Physics and Controlled Fusion*, **57**, 095008.
[20] S R Haskey *et al*, 2014, *Plasma Physics and Controlled Fusion*, **56**, 035005.
[21] Y Q Liu *et al*, 2000, *Physics of Plasmas*, **7**, 3681.
[22] D A Ryan *et al*, 2017, *Plasma Physics and Controlled Fusion*, **59**, 024005.
[23] P Piovesan *et al*, 2017, *Plasma Physics and Controlled Fusion*, **59**, 014027.
[24] P Berens, 2009, *Journal of Statistical Software*, **31**.
[25] W Suttrop *et al*. Physical Description of External Circuitry for Resistive Wall Mode Control in ASDEX Upgrade. In *36th EPS Conference on Plasma Physics*, P1.165, 2009.
[26] M Willensdorfer *et al*, 2016, *Plasma Physics and Controlled Fusion*, **58**, 114004.
[27] C.J. Ham *et al*, 2016, *Nuclear Fusion*, **56**, 086005.
[28] H Lütjens *et al*, 1996, *Computer Physics Communications*, **97**, 219–260.
[29] ITER. ABT4ZL version 1.0. Private communication, 2012.
[30] T Casper *et al*, 2014, *Nuclear Fusion*, **54**, 013005.
[31] L Li *et al*, 2017, *Plasma Physics and Controlled Fusion*, **59**, 044005.
[32] Y Liu *et al*, 2015, *Nuclear Fusion*, **55**, 063027.
[33] T E Evans *et al*, 2013, *Nuclear Fusion*, **53**, 093029.
[34] J A Crotinger, 1997, *Lawrence Livermore National Laboratory Technical Report UCRL-ID-126284*.
[35] B C Lyons *et al*, 2017, *Plasma Physics and Controlled Fusion*, **59**, 044001.

[36] N Leuthold *et al*, 2017, *Plasma Physics and Controlled Fusion*, **59**, 055004.
[37] A Kirk *et al*, 2013, *Plasma Physics and Controlled Fusion*, **55**, 045007.